Received: 1 April 2023 | Revised: 8 June 2023 | Accepted: 22 June 2023

DOI: 10.1111/jace.19320

Journal of the American Ceramic Society

RESEARCH ARTICLE

Crystal growth and phase formation of high-entropy rare-earth monoclinic aluminates

Matheus Pianassola[1,2,3] | **Madeline Loveday**[2] | **Rebecca Lalk**[1,2] | **Kimberly Pestovich**[1,2] | **Charles L. Melcher**[1,2,4] | **Mariya Zhuravleva**[1,2]

[1]Scintillation Materials Research Center, University of Tennessee, Knoxville, Tennessee, USA

[2]Department of Materials Science and Engineering, University of Tennessee, Knoxville, Tennessee, USA

[3]Saint-Gobain Research North America, Northborough, Massachusetts, USA

[4]Department of Nuclear Engineering, University of Tennessee Knoxville, Knoxville, Tennessee, USA

Correspondence
Matheus Pianassola, Scintillation Materials Research Center, University of Tennessee, Knoxville, TN 37996, USA.
Email: mpianass@vols.utk.edu

Funding information
National Science Foundation, Grant/Award Number: DMR 1846935

Abstract

For the first time, high-entropy rare-earth monoclinic aluminate crystals were grown via directional solidification using the micro-pulling-down method. Five high-entropy compositions were formulated with a general formula $RE_4Al_2O_9$, where RE is an equiatomic mixture of five rare-earth elements. The rare-earth elements included were Lu, Yb, Er, Y, Ho, Dy, Tb, Gd, Eu, Sm, Nd, and La. High-temperature powder X-ray diffraction and Rietveld structure refinement indicated that all crystals were a single monoclinic phase and that rare-earth average ionic radius did not affect phase purity. At room temperature, the refined lattice parameters increased consistently with increasing average ionic radii of the five compositions. One of the crystals had a typical high-temperature phase transition of single-RE $RE_4Al_2O_9$ in the range of 1100–1150°C, which consisted of a lattice contraction upon heating. Differential scanning calorimetry indicated a thermal event corresponding to that phase transition. Electron probe microanalysis revealed Al-rich inclusions on the surface of the crystals. Crystals containing Tb had dark surface features that became lighter after annealing in a reducing atmosphere, which indicated that Tb^{4+} may be responsible for the dark features.

KEYWORDS
aluminates, crystal growth, rare earths

1 | INTRODUCTION

Rare-earth (RE) aluminates have been extensively investigated for luminescence applications.[1,2] Garnets, perovskites, and monoclinic aluminates are typically formed in the RE_2O_3-Al_2O_3 systems and their general formula are $RE_3Al_5O_{12}$, $REAlO_3$, and $RE_4Al_2O_9$, respectively.[3,4] Among those three general compounds, several garnet and perovskite aluminate single crystals are commercialized for scintillation and laser applications, including $Lu_3Al_5O_{12}$ and $YAlO_3$, doped with luminescent activators such as Ce^{3+} and Nd^{3+} [1,5] On the other hand, the exploration and practical application of monoclinic aluminate single crystals remains relatively limited. All REs and Y form thermodynamically stable $RE_4Al_2O_9$ (space group $P2_1/c$), except for Nd, Pr, Ce, and La.[4] Here, Y is referred to as a RE for simplicity.

A high-temperature solid-solid phase transition prevents the growth of high optical quality monoclinic aluminate single crystals via directional solidification methods. Previous high-temperature X-ray diffraction (XRD) and thermal analysis studies revealed that single-RE monoclinic aluminates undergo a diffusionless, martensitic phase transition.[6–10] The crystallographic space group of the low- and high-temperature phases are identical ($P2_1/c$), but the unit cell volume of the

high-temperature phase is ~0.4% smaller than that of the low-temperature phase. The phase transition temperature increases with decreasing RE^{3+} ionic radius from $Sm_4Al_2O_9$ to $Yb_4Al_2O_9$ in the temperature range of 1000–1300°C.[10] Although the ionic radius of Y^{3+} is similar to that of Ho^{3+},[11] $Y_4Al_2O_9$ has a significantly higher transition temperature (1377°C) than $Ho_4Al_2O_9$ (1219°C).[10] This phase transition results in internal stress in crystals grown from the melt, leading to cracking upon cooling as well as polycrystallinity at room temperature, as demonstrated by previously published growth experiments.[12–14] For these reasons, the fundamental and luminescent properties of $RE_4Al_2O_9$ are mainly investigated in the polycrystalline form.[15–18]

The effects of the high-entropy compositional approach on the optical quality of monoclinic aluminate crystals have not yet been evaluated. Such a compositional approach is inspired by high-entropy alloys[19] and consists of admixing five or more cations in equiatomic amounts to fractionally occupy cation sublattices.[20] Entropy-driven phase stabilization and synergistic effects on functional properties have been reported for high-entropy oxides.[21] To the best of our knowledge, only one high-entropy monoclinic aluminate has been reported and no crystal growth results were presented. A $(Nd,Sm,Eu,Y,Yb)_4Al_2O_9$ polycrystalline ceramic was evaluated for environmental barrier applications, and no phase transitions were observed up to 1200°C,[22] which is an indication that the high-entropy design could contribute to the phase stability of RE monoclinic aluminates. Additionally, suppression of polymorphic transitions in complex RE sesquioxides (RE_2O_3) has been previously attributed to the high-entropy compositional approach.[23,24] This inspires the investigation of the crystal growth of high-entropy $RE_4Al_2O_9$ since high optical quality and attractive luminescence properties could be achieved if the lattice expansion upon cooling is suppressed.

In this work, we demonstrate crystal growth of high-entropy $RE_4Al_2O_9$ for the first time, contributing to the emerging field of crystal growth of high-entropy oxides.[24–34] The phase formation and optical quality of crystals containing five REs, including Lu, Yb, Er, Y, Ho, Dy, Tb, Gd, Eu, Sm, Nd, and La were evaluated. Our composition formulation strategy used the RE^{3+} average ionic radius (AIR) as a parameter to evaluate its effects on phase formation and optical quality. Crystals were grown via directional solidification using the micro-pulling-down (mPD) method, which is ideal for materials development research due to its fast growth rates (up to 20 mm/min) and low consumption of starting material (~1 g).[35] High-temperature structural stability was evaluated via powder XRD and transition temperatures were identified via differential scanning calorimetry (DSC).

TABLE 1 List of rare-earth cations and their respective atomic number, ionic radius for coordination number VI, [11] and size classification.

RE^{3+} cation	Atomic number	RE^{3+} ionic radius (Å)	Size classification
Lu^{3+}	71	0.848	Small
Yb^{3+}	70	0.858	Small
Er^{3+}	68	0.881	Small
Y^{3+}	39	0.892	Small
Ho^{3+}	67	0.894	Small
Dy^{3+}	66	0.908	Medium
Tb^{3+}	65	0.923	Medium
Gd^{3+}	64	0.938	Medium
Eu^{3+}	63	0.950	Medium
Sm^{3+}	62	0.964	Medium
Nd^{3+}	60	0.995	Large
La^{3+}	57	1.061	Large

2 | METHODS

2.1 | Composition formulation

To study the potential effect of the average ionic radius (AIR) on the phase formation of high-entropy $RE_4Al_2O_9$, the ionic radii of the RE^{3+} cations were considered for composition formulation. Table 1 lists the REs included in the compositions, their atomic number, respective ionic radii (IR), and their IR classification. The IR classification was designed to classify the cations into small, medium, or large in terms of their ionic radius. To do so, we took the difference in the ionic radius of the largest and smallest RE^{3+} in Table 1; this difference is 0.213 Å. We then divided 0.213 Å by 3 which results in 0.071 Å and used this value to generate three IR ranges starting from the IR of the smallest RE^{3+}, namely Lu^{3+} (0.848 Å). The three IR ranges are 0.848–0.919 Å (small), 0.920–0.991 Å (medium), and 0.992–1.063 Å (large). Five high-entropy $RE_4Al_2O_9$ compounds were formulated, each containing five REs in equiatomic amounts. The five compositions, their respective ID number, and average ionic radius (AIR) are listed in Table 2. The AIR values increase consistently from compositions 1 to 5. Composition 1 has only small REs; composition 2 has a mixture of small and medium REs; compositions 3 and 5 have a mixture of small, medium, and large REs; and composition 4 has a mixture of medium and large REs.

TABLE 2 List of high-entropy $RE_4Al_2O_9$ compositions, their ID, and respective average ionic radius (AIR)[11]. Commas indicate equiatomic amounts.

ID	Composition	AIR (Å)
1	$(Lu,Yb,Er,Y,Ho)_4Al_2O_9$	0.875
2	$(Lu,Yb,Y,Tb,Gd)_4Al_2O_9$	0.892
3	$(Yb,Y,Gd,Sm,Nd)_4Al_2O_9$	0.929
4	$(Dy,Tb,Gd,Eu,Sm)_4Al_2O_9$	0.937
5	$(Er,Dy,Gd,Sm,La)_4Al_2O_9$	0.950

2.2 | Crystal growth

The micro-pulling-down method[35] was used to grow ∅ 3 mm cylindrical crystals. A KDN Dai-Ichi Kiden growth station was used with an RF generator model TR-02001 operated at 26 kVA. A ∅16 mm iridium crucible with a ∅3 mm die and a ∅0.5 mm capillary channel was used as the melt reservoir. The starting materials were Lu_2O_3, Yb_2O_3, Er_2O_3, Y_2O_3, Ho_2O_3, Dy_2O_3, Tb_2O_3, Gd_2O_3, Eu_2O_3, Sm_2O_3, Nd_2O_3, La_2O_3, and Al_2O_3 powders of at least 99.99% purity. A list of starting powder, manufacturer, and purity is in Table S1 in the Supplementary Material. The powders were dried at 800°C for 8 h in air, mixed in stoichiometric ratios, and placed in the crucible. The powder mixtures were melted by inductively heating the crucible. An iridium pin was used as a seed to initiate the growth by touching the bottom outlet of the crucible capillary channel and pulling down the melt. All crystals were grown with a pulling rate of 0.10 mm/min. Details about the mPD growth method and the crystal growth setup used here can be found in a previous publication.[25]

2.3 | Differential scanning calorimetry

To identify any thermal events that could be correlated to phase transitions, DSC curves were obtained with a Labsys EVO-TG-DSC 1600 instrument. The crystals were crushed to a fine powder with a mortar and pestle and placed in alumina crucibles. A heating and a cooling rate of 5°C/min were used to collect data from room temperature to 1300°C in air. The gas flow is not a variable option in this DSC instrument and the instrument manual indicates that the gas flow is a few liters per hour.

2.4 | Powder XRD

Phase analysis of all crystals was investigated at room-temperature via powder XRD. The middle section of each crystal was cut and ground into a fine powder in a mortar. A Panalytical Empyrean diffractometer was used to collect diffraction patterns in the Bragg-Brentano geometry using a Cu Kα X-ray source at 45 kV and 40 mA. The incident X-ray beam passed through the following optics: 0.04 rad Soller slits, a 1/4° divergence slit, a 10 mm fixed beam mask, and a 1/2° anti-scatter slit. The diffracted X-ray beam passed through the following optics: a 1/4° anti-scatter slit, 0.04 rad Soller slits, and a nickel beta filter. A PIXcel3D detector was used to collect the diffraction patterns. Patterns were collected in the 2θ range of 20–70° using a 0.0131° step size. The patterns were used to determine the phase composition and lattice parameters via Rietveld structure refinements performed with the General Structure Analysis System II software (GSASII).[36] The input structure was that of $Tb_4Al_2O_9$ (ICSD # 164882) and the Tb^{3+} cations were substituted with the five REs of the corresponding composition, each with a 1/5 fractional occupation.

Crystals 4 and 5 were subjected to high-temperature powder XRD using the diffraction instrument and optics described in the previous paragraph and an HTK 1200N high-temperature stage from Malvern Panalytical. Patterns were collected in increments of 100°C upon heating at a rate of 5°C/min in the range of 100–1200°C. An additional measurement was performed at 1150°C for crystal 4 to narrow down the temperature range in which a phase transition lies. Patterns were collected in the 2θ range of 8–65° using a 0.0066° step size. The patterns were used to determine the lattice parameters via Rietveld structure refinements with GSASII.[36] The refined variables were sample displacement, lattice parameter, microstrain, and preferred orientation (spherical harmonic model, harmonic order 8–12).

2.5 | Annealing experiments

To study the effects of reducing annealing on surface features, crystals were annealed in a flowing atmosphere of 2% H_2 in bulk N_2 at 1300°C for 8 h. Subsequently, the same samples were subjected to oxidizing annealing in air at 1300°C for 8 h. A tubular CM High Temperature Furnace model 1630-12 was used for these experiments. A gas flow rate of ~5 liters per minute was used.

2.6 | Electron probe microanalysis

To evaluate the microstructure and composition of the crystals, small fragments (<1 mm^3) of the crystals were embedded in epoxy and polished. The samples were then

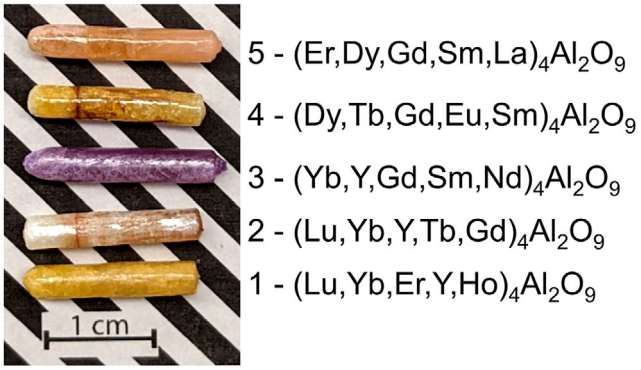

FIGURE 1 Photo of the high-entropy $RE_4Al_2O_9$ crystals. Composition ID is indicated in the figure and refers to the composition in Table 2. Crystals are 3 mm in diameter and were grown with good shape control. All crystals were polycrystalline at room temperature.

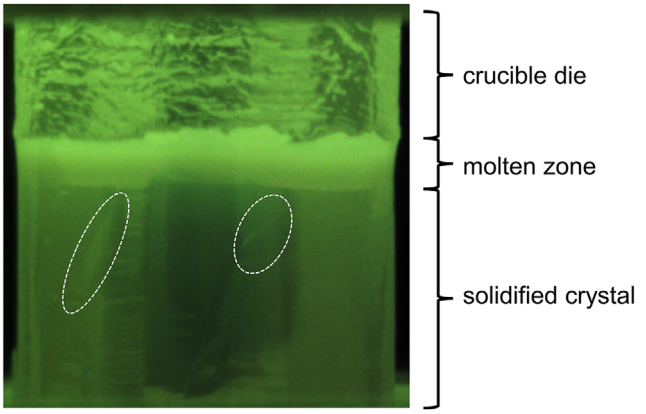

FIGURE 2 In situ photo of growth of Crystal 2 $(Lu,Yb,Y,Tb,Gd)_4Al_2O_9$. The iridium crucible die, molten zone, and solidified crystal are indicated in the figure. In the solidified crystal, cracks are indicated by white ovals. The darker central region in the crystal indicates translucency as the camera captures the darker background through the crystal.

imaged and analyzed via electron probe microanalysis (EPMA) with a CAMECA SX100 Electron Microprobe operated at 15 kV and 30 nA. The instrument is equipped with high-speed backscattered electron (BSE) detectors and four wavelength-dispersive spectrometers (WDS). The probe point size was 1 μm, and the excitation area diameter was in the 2–3 μm range.

3 | RESULTS AND DISCUSSION

3.1 | Grown crystals

Uniform diameter control was achieved for all grown crystals, pictured in Figure 1. Crystals with compositions 1 and 4 are yellow due to Ho^{3+}, Dy^{3+}, and Sm^{3+}. Crystal 2 was expected to be white since the constituent RE^{3+} cations form whiteish aluminates; however, dark brown features are seen on the surface of Crystal 2. Such features are also seen on Crystal 4 and will be discussed in Section 3.5. Crystal 3 is purple due to Nd^{3+}. Crystal 5 has a salmon color due to the presence of Er^{3+} and Sm^{3+} cations, which form pink and yellow oxides, respectively.

All crystals were translucent during growth and polycrystalline after cooling to room temperature. A picture obtained during the growth of Crystal 2 is in Figure 2. The darker central region in the growing crystal indicated translucency, as the camera captures the dark background through the crystal. Similar indications of translucency were observed during the growth of all crystals in this study. Cracks in Crystal 2 are indicated by white ovals in Figure 2. There are two possible explanations for the polycrystallinity at room temperature; (1) the crystals underwent a phase transition upon cooling leading to residual stress and cracking; and (2) the growth parameters used here (thermal gradient, pulling rate, cooling rate) were not optimized for the growth of monoclinic aluminates. Regarding explanation 2, it is important to note that the growth parameters used here were similar to the ones used to previously grow high-entropy garnet and perovskite aluminates.[25,30,31]

3.2 | Structural analysis via room temperature powder XRD

Crystals 1–5 were a single monoclinic phase (space group $P2_1/c$) according to room temperature powder XRD and Rietveld structure refinement, and their AIR did not affect phase formation. An example of a refinement fit is shown in Figure S1 in the Supplementary Material for crystal 5. Diffraction patterns of the five crystals and reference patterns of $Lu_4Al_2O_9$ (small IR) and $Sm_4Al_2O_9$ (medium IR) are compared in Figure 3. The reference patterns indicate that the diffraction peaks shift to smaller two-theta values for larger REs, which is expected due to an enlargement of the unit cell.

The relative position of the powder XRD reflection peaks varies with crystal AIR, which is also observed in single-RE $RE_4Al_2O_9$. As indicated in Figure 3, around 30°, the order or the reflection peaks for $Lu_4Al_2O_9$ going from small to large two-theta is $(22\bar{1})$, (023), (032), (211), and $(\bar{2}13)$. For $Sm_4Al_2O_9$ the order of these peaks is $(22\bar{1})$, (211, (032), (023), and $(\bar{2}13)$. The relative distance between these peaks also varied. This explains why the collected patterns look different around 30° as the AIR increases from Crystal 1 to Crystal 5

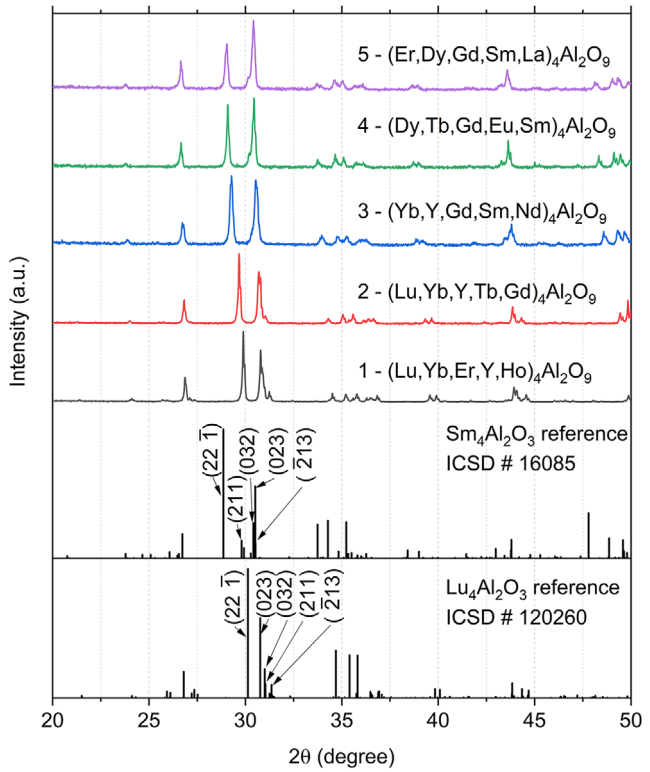

FIGURE 3 Powder XRD patterns of crystals 1–5 and reference patterns of $Lu_4Al_2O_9$ and $Sm_4Al_2O_9$ (space group $P2_1/c$). Crystal ID and compositions are seen in Table 2.

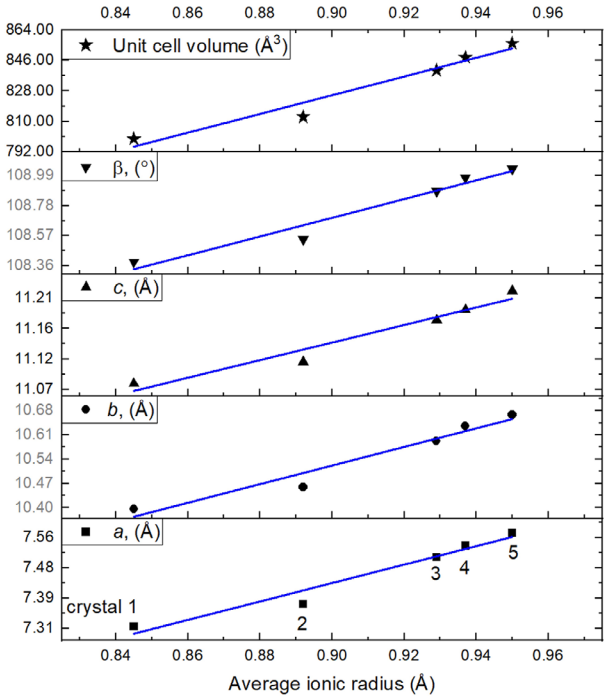

FIGURE 4 Lattice parameters of Crystals 1–5 obtained with powder XRD and Rietveld refinement. The crystal ID at the bottom graph applies to all graphs and compositions are seen in Table 2. Linear regression lines are shown for each data set ($R^2 = 94\%$ for all regressions).

In terms of peak intensity, the (22$\bar{1}$) reflection peak becomes less intense than the (023) peak as the AIR increases from crystal 1 to 5, which may be correlated with the type or RE contained on those crystallographic planes. Similar peak intensity variation with composition has been observed in other high-entropy oxides and was correlated with the atomic scattering factor of the constituent cations.[37,38] The atomic scattering power of X-rays is directly proportional to the atomic number.[39] This indicates that with the enlargement of the unit cell from crystals 1 to 5, atoms with larger atomic numbers (and smaller IR, see Table 1) tend to occupy the crystallographic sites that lie in the (023) plane rather than the (22$\bar{1}$) plane. Figure S2 in the Supplementary Material includes a schematic representation of both planes in the monoclinic unit cell. Since XRD is not suitable for distinguishing between rare-earth elements, further structural characterization with neutron diffraction is needed to determine the specific cationic distribution in the crystallographic lattice.[40]

Rietveld refinement results indicated that the crystallographic lattice parameter values of Crystals 1–5 increased consistently with their AIR. As seen in Figure 4, the three lattice parameters (a, b, and c) increased nearly linearly with increasing AIR from Crystal 1 to 5. The β angle formed between the a- and c-axis also increases with the AIR, as shown in Figure 4. Consequently, the unit cell volume also increases with AIR. This consistent variation of lattice parameters with AIR has been previously observed in high-entropy garnet aluminate crystals grown by the micro-pulling-down method.[30]

3.3 | Thermal analysis via DSC

A thermal event at ~1150°C indicates that Crystal 4 may undergo a high-temperature phase transition. The five crystals were subjected to DSC measurements to identify any thermal events that may be correlated with phase transitions, as has been previously reported for $Y_4Al_2O_9$.[7] The heat flow curves obtained upon heating and cooling are in Figure 5A,B, respectively. Only crystal 4 had a consistent thermal event that appeared as an endothermic peak upon heating (~1130°C) and an exothermic peak upon cooling (~1045°C). These thermal events are indicated with dashed ovals in Figure 5A,B and are in the temperature range of the typical high-temperature phase transition of single-RE $RE_4Al_2O_9$, 1000–1380°C.[10] High-temperature structural analysis studies are presented in Section 3.4 to confirm whether Crystal 4 undergoes a

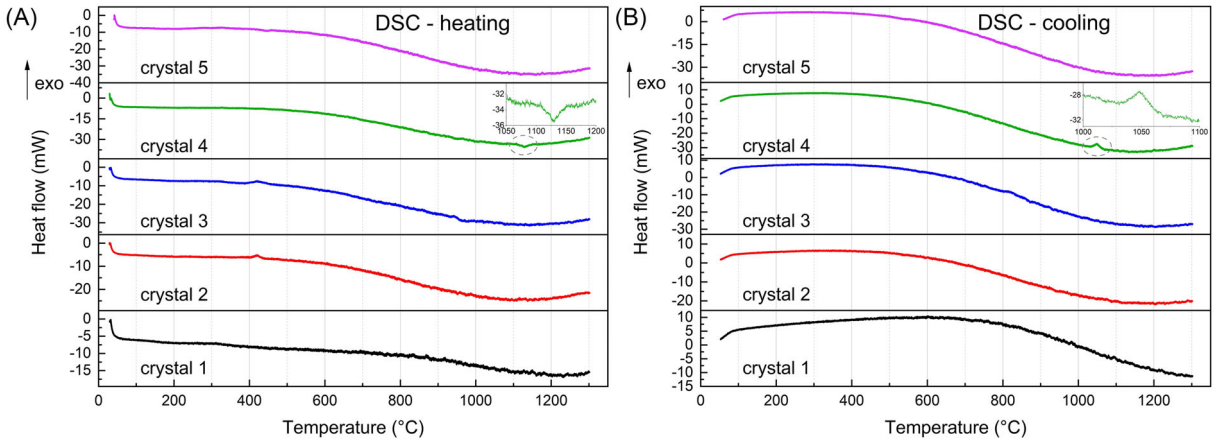

FIGURE 5 DSC curves obtained upon (A) heating (B) and cooling. Thermal events correlated to high-temperature phase transitions in crystal 4 are indicated with dashed ovals.

phase transition. A few other features were in the heating profiles at ~425°C for Crystals 2 and 3, and at ~950°C for Crystal 4 (Figure 5A). These features are likely to be due to instrumental effects and do not have a corresponding event in the cooling curves.

3.4 | Structural analysis via high-temperature powder XRD

A high-temperature lattice contraction upon heating was detected for Crystal 4 via powder XRD. Crystal 4 was selected for high-temperature phase analysis due to the thermal events identified in DSC (Section 3.2). Crystal 5 was also selected due to the high concentration of larger REs (Tables 1 and 2), which form single-RE $RE_4Al_2O_9$ with a lower phase transition temperature.[10] This high concentration could potentially minimize the transition temperature of the high-entropy compounds, allowing the detection via high-temperature powder XRD. All diffraction patterns collected for Crystals 4 and 5 could be successfully used for structure refinement with a space group $P2_1/c$, which has been previously reported for single-RE $RE_4Al_2O_9$.[6–10] Refinement results for Crystals 4 and 5 are seen in Tables S2 and S3 in the Supplementary Material, respectively. The normalized refined lattice parameters of Crystals 4 and 5 are seen in Figure 6A, B, respectively.

Crystal 4 undergoes a lattice contraction upon heating between 1100 and 1150°C, as seen in Figure 6A. This phase transition results in the contraction of lattice parameters *a* and *b*, and the expansion of lattice parameter *c*. This is consistent with the previously reported structural studies on single-RE $RE_4Al_2O_9$.[6–10] Such phase transition is not observed in crystal 5 and their lattice parameters increase monotonically from room temperature to 1300°C as seen in Figure 6B.

Depending on the composition, the high-entropy compositional approach may extend the temperature range of structural stability in $RE_4Al_2O_9$ compounds. Both Crystal 5 and the previously reported $(Nd,Sm,Eu,Y,Yb)_4Al_2O_9$[22] are structurally stable from room temperature to 1200°C. This is surprising since the lowest transition temperature for single-RE $RE_4Al_2O_9$ is 1044°C for $Sm_4Al_2O_9$.[10] On the other hand, Crystal 4 has a phase transition temperature (1100–1150°C) within the temperature range in which phase transitions happens in single-RE $RE_4Al_2O_9$ (1000–1300°C). To determine how composition affects the structural stability of high-entropy $RE_4Al_2O_9$, further structural investigation on Crystals 1, 2, 3, and 5 above the maximum temperature of the structural analysis performed here (1200°C) is needed. Measurements up to temperatures close to the melting point of these compounds would be advisable to capture the full dependence of the structural behavior on temperature. Maximum experimental temperatures around 2100°C would be required since the melting points of single-RE $RE_4Al_2O_9$ are in the range of 1950–2040°C,[4] and the melting points of high-entropy oxides is usually lower or similar to their single-cation analogous oxides.[24,41,42] Such extreme temperature measurements require careful treatment to avoid reactions between the sample and sample holder. One strategy to perform these measurements is to use a containerless sample environment. Aerodynamic levitation and laser heating have been previously used to perform high-temperature neutron and XRD on high-entropy oxides.[24,41,43–47]

3.5 | Dark surface features in crystals 2 and 4

To determine the nature of the dark surface features in Crystals 2 and 4, EPMA data were collected and indicated

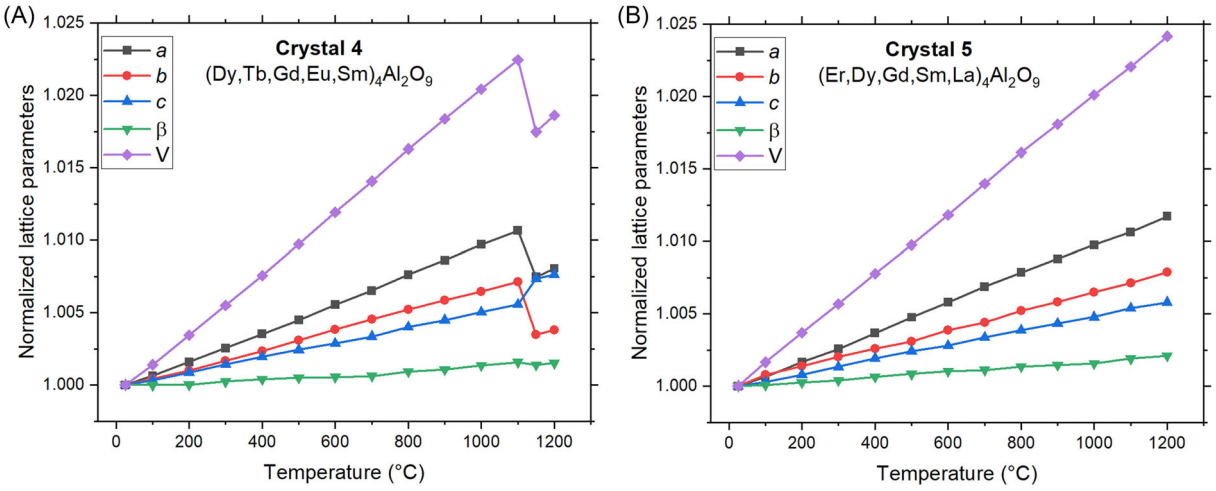

FIGURE 6 Normalized lattice parameter for Crystals (A) 4 and (B) 5. Lattice parameters were obtained from Rietveld refinement using powder XRD patterns. In the legend, V stands for unit cell volume.

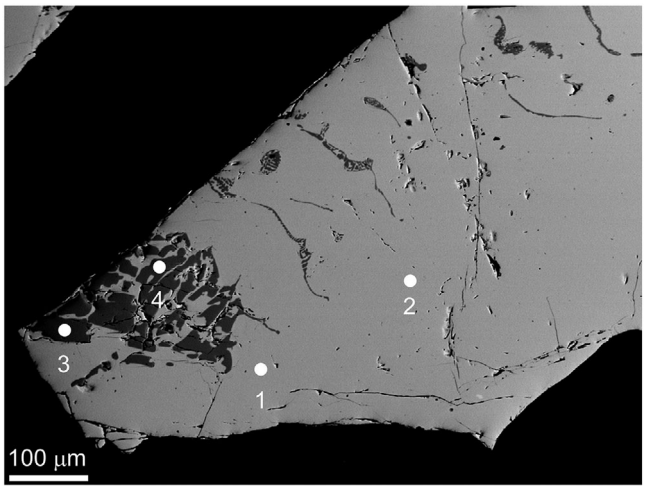

FIGURE 7 Micrograph of crystal 2 obtained via back-scattered electron imaging using an EPMA instrument. The chemical composition of points 1–4 is presented in Table 3.

aluminum-rich inclusions on the outer surface of Crystal 2. In general, the composition characterization of the crystals was challenging due to their brittleness, which hindered appropriate sample preparation such as cutting and polishing. A back-scatter electron image of a surface fragment of Crystal 2 is shown in Figure 7. Dark inclusions were seen in the matrix; the measured composition of points 1–4 indicated in Figure 7 is presented in Table 3. The dark inclusions (points 3 and 4) were richer in aluminum compared to the matrix (points 1 and 2). Similar Al-rich inclusions were previously seen on the surface of micro-pulling-down RE garnet aluminates.[30,31] In back-scattered electron imaging, the higher the atomic number of the atoms probed the brighter the image. This explains why the matrix in Figure 7 is brighter than the Al-rich inclusions since the concentration of REs (higher atomic numbers) is relatively higher in the matrix.

It is not likely that the inclusions seen in Figure 7 correspond to the dark surface features of Crystal 2. The dark, aluminum-rich inclusions observed in the back-scattered electron image would not be dark when seen by the naked eye. This is because Al_2O_3 is white and the mixture of the trivalent constituent REs in this composition would result in a light-yellow color. Therefore, it is likely that the dark features on the crystal surface result from tetravalent REs such as Tb^{4+}, since oxides containing Tb^{4+} are dark. In this case, such features would not be distinguishable in back-scattered electron imaging because the image contrast arises from gradients of atomic numbers, not oxidation states.

The dark surface features may be related to composition and the presence of Tb^{4+}. Both Crystals 2 and 4 are the only ones containing Tb in their composition (Table 2). Among all the REs included in this study (Table 1), only Tb commonly assumes the 4+ oxidation state, which leads to a characteristic dark color. To test this proposed explanation, fragments from the tail end of Crystal 2 and the seed end of Crystal 4 were subjected to reducing annealing to check for color changes. As shown in Figure 8, a lighter color was seen on the surface of the crystals after the reducing annealing. The same samples were subsequently subjected to oxidizing annealing and the surface features became darker. This supports the proposed explanation for the nature of the dark surface features as a fraction of the Tb^{4+} may have been reduced during the first annealing leading to lighter surface color. A fraction of the Tb^{3+} ions may have oxidized during the second annealing, leading to darker surface features.

TABLE 3 EPMA elemental composition data for crystal 2. Points 1–4 correspond to the areas indicated in Figure 7.

		EPMA elemental composition (at%), error < 0.001 at%							
Area	**Points from Figure 7**	**Lu**	**Yb**	**Y**	**Tb**	**Gd**	**Al**	**O**	**Stoichiometry**
	Nominal composition	*5.3*	*5.3*	*5.3*	*5.3*	*5.3*	*13.3*	*60*	$RE_4Al_2O_9$
Lighter matrix	1	5.8	6.5	5.3	5.9	5.1	11.3	60.1	$RE_{4.1}Al_{1.6}O_{8.6}$
	2	5.9	6.4	5.0	5.8	5.8	11.0	60.1	$RE_{4.1}Al_{1.6}O_{8.6}$
Darker areas	3	3.5	4.0	3.4	5.0	5.4	18.8	59.9	$RE_{3.0}Al_{2.7}O_{8.6}$
	4	3.0	3.6	3.3	5.3	5.9	18.9	60.0	$RE_{3.0}Al_{2.7}O_{8.6}$

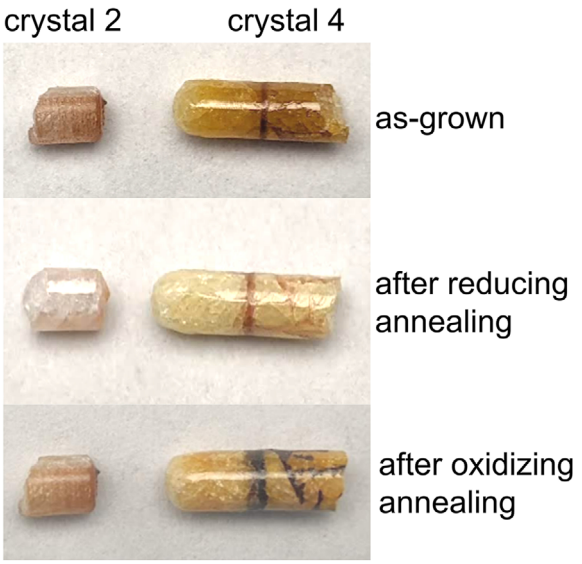

FIGURE 8 Samples from crystals 2 and 4 in the as-grown condition and after reducing and subsequent oxidizing annealing. The sample from crystal 2 is from the tail end, while the sample from crystal 4 is from the seed end. Crystals are 3 mm in diameter.

Tetravalent Tb may have originated from the raw materials or the oxidation of Tb^{3+} during growth. The source of Tb in this study is Tb_2O_3, in which Tb is nominally in the 3+ oxidation state; however, the raw powder may have contained some amount of Tb^{4+} as a result of the spontaneous oxidation of the powder stored in air. Additionally, Tb^{3+} may have been converted into Tb^{4+} during growth, even though the growth atmosphere was inert. This is because Crystals 2 and 4 contain Yb and Eu, respectively, which can assume the 2+ oxidation state. Therefore, redox reactions could have happened during the growth. These reactions would be $Tb^{3+} \rightarrow Tb^{4+} + e^-$ and $Yb^{3+} + e^- \rightarrow Yb^{2+}$ or $Eu^{3+} + e^- \rightarrow Eu^{2+}$. Such redox reactions have been previously observed in oxide materials.[48,49]

4 | CONCLUSION

For the first time, high-entropy monoclinic aluminate crystals were grown via directional solidification by the micro-pulling-down method. Compositions containing a combination of five REs in equiatomic amounts were formulated to determine the effects of AIR on phase formation. All the grown crystals successfully formed a single monoclinic phase. All crystals were translucent during growth and polycrystalline at room temperature, which was likely due to a lattice expansion upon cooling that is typical of single-RE monoclinic aluminates. Differential scanning calorimetry allowed the identification of a high-temperature thermal event for Crystal 4 $(Dy,Tb,Gd,Eu,Sm)_4Al_2O_9$ while the other four crystals did not have any significant thermal events. High-temperature powder XRD was instrumental to identify a lattice contraction upon heating for Crystal 4 in the range of 1100–1150°C, while the unit cell of Crystal 5 $(Er,Dy,Gd,Sm,La)_4Al_2O_9$ expanded monotonically. Dark surface features in Tb-containing crystals may be related to the presence of Tb^{4+} ions in the compounds.

Future investigation is needed to explore the structural behavior of high-entropy $RE_4Al_2O_9$ above 1200°C. This would indicate whether the polycrystallinity seen in Crystals 1, 2, 3, and 5 at room temperature is due to phase transitions that could not be identified due to operating temperature limitations, or if it is a result of nonoptimized crystal growth parameters such as growth or cooling rates. Nevertheless, the present study demonstrates that the high-entropy compositional approach extends the temperature range of structural stability in $RE_4Al_2O_9$ compounds since a phase transition was only detected for one of the five crystals. This makes such complex aluminates attractive for high-temperature applications such as thermal environmental barriers, as previously suggested.[20] Additionally, this work inspires the investigation of functional properties in high-entropy polycrystalline samples since single-phase compounds were successfully produced with a variety of RE combinations.

ACKNOWLEDGMENTS

This work was supported by the National Science Foundation (grant number: DMR 1846935). Powder XRD was performed at the Institute for Advanced Materials and Manufacturing (IAMM) Diffraction Facility, located at the

University of Tennessee, Knoxville. Electron microprobe measurements were performed at the Electron Microprobe Laboratory in the Department of Earth and Planetary Sciences at the University of Tennessee, Knoxville with the assistance of Molly McCanta and Allan Patchen.

ORCID

Matheus Pianassola https://orcid.org/0000-0001-7468-2794

Rebecca Lalk https://orcid.org/0000-0001-6993-6438

REFERENCES

1. Nikl M, Yoshikawa A, Kamada K, Nejezchleb K, Stanek CR, Mares JA, et al. Development of LuAG-based scintillator crystals - a review. Prog Cryst Growth Charact Mater. 2013, 59(2):47–72. https://doi.org/10.1016/j.pcrysgrow.2013.02.001
2. Ikesue A, Aung YL, Taira T, Kamimura T, Yoshida K, Messing GL. Progress in ceramic lasers. Annu Rev Mater Res. 2006, 36(3):397–429. https://doi.org/10.1146/annurev.matsci.36.011205.152926
3. Mao H, Selleby M, Fabrichnaya O. Thermodynamic reassessment of the Y 2O3-Al2O3-SiO2 system and its subsystems. Calphad Comput Coupling Phase Diagrams Thermochem. 2008, 32(2):399–412. https://doi.org/10.1016/j.calphad.2008.03.003
4. Wu P, Pelton AD. Coupled thermodynamic-phase diagram assessment of the rare earth oxide-aluminium oxide binary systems. J Alloys Compd. 1992, 179(1–2):259–87. https://doi.org/10.1016/0925-8388(92)90227-Z
5. Schwarz F, Aoki A, Becker J, Sculean A. Laser application in non-surgical periodontal therapy: a systematic review. J Clin Periodontol. 2008, 35(SUPPL. 8):29–44. https://doi.org/10.1111/J.1600-051X.2008.01259.X
6. Yamane H, Shimada M, Hunter BA. High-temperature neutron diffraction study of Y4Al2O9. J Solid State Chem. 1998, 141(2):466–74. https://doi.org/10.1006/JSSC.1998.7998
7. Yamane H, Omori M, Okubo A, Hirai T. High-temperature phase transition of Y4Al2O9. J Am Ceram Soc. 1993, 76(9):2382–4. https://doi.org/10.1111/J.1151-2916.1993.TB07783.X
8. Yamane H, Ogawara K, Omori M, Hirai T. Thermal expansion and athermal phase transition of Y4AI2O9 ceramics. J Am Ceram Soc. 1995, 78(5):1230–2. https://doi.org/10.1111/J.1151-2916.1995.TB08474.X
9. Gervais M, Douy A. Solid phase transformation and melting of the compounds Ln4Al2O9 (Ln = Gd, Dy, Y). Mater Sci Eng B. 1996, 38(1–2):118–21. https://doi.org/10.1016/0921-5107(95)01322-9
10. Yamane H, Ogawara K, Omori M, Hirai T. Phase transition of rare-earth aluminates (RE4Al2O9) and rare-earth gallates (RE4Ga2O9). J Am Ceram Soc. 1995, 78(9):2385–90. https://doi.org/10.1111/j.1151-2916.1995.tb08673.x
11. Shannon RD, Prewitt CT. Effective ionic radii in oxides and fluorides. Acta Crystallogr Sect B Struct Crystallogr Cryst Chem. 1969, 25(5):925–46. https://doi.org/10.1107/s0567740869003220
12. Okada G, Akatsuka M, Kimura H, Mori M, Kawano N, Kawaguchi N, et al. Characterizations of Ce-doped Y 4 Al 2 O 9 crystals for scintillator applications. Sensors Mater. 2018, 30(7):1547–54. https://doi.org/10.18494/SAM.2018.1919
13. Boruc Z, Fetlinski B, Kaczkan M, Turczynski S, Pawlak D, Malinowski M. Temperature and concentration quenching of Tb3+ emissions in Y4Al2O9 crystals. J Alloys Compd. 2012, 532:92–7. https://doi.org/10.1016/J.JALLCOM.2012.04.017
14. Drozdowski W, Witkowski ME, Brylew K, Łachmański W, Makowski M, Wojtowicz AJ, et al. A preliminary assessment of Lu2Y2Al2O9:Pr (LuYAM:Pr) as a potential scintillator. Radiat Meas. 2016, 93:41–5. https://doi.org/10.1016/j.radmeas.2016.06.009
15. Wang Y, Hrubiak R, Turczyński S, Pawlak DA, Malinowski M, Włodarczyk D, et al. Spectroscopic properties and martensitic phase transition of Y4Al2O9:Ce single crystals under high pressure. Acta Mater. 2019, 165:346–61. https://doi.org/10.1016/J.ACTAMAT.2018.11.057
16. Kaczkan M, Turczyński S, Pawlak DA, Wencka M, Malinowski M. Laser site-selective spectroscopy of Eu3+ ions doped Y4Al2O9. Opt Mater (Amst). 2016, 58:412–7. https://doi.org/10.1016/J.OPTMAT.2016.06.023
17. Xia G, Zhou S, Zhang J, Wang S, Wang H, Xu J. Sol–gel combustion synthesis and luminescence of Y4Al2O9:Eu3+ nanocrystal. J Non Cryst Solids. 2005, 351(37–39):2979–82. https://doi.org/10.1016/J.JNONCRYSOL.2005.07.007
18. Huang Y, Jang K, Wang X, Xian G, Cho E, Lee HS, et al. The luminescence of Pr3+ ions doped in Y4Al2O9 by sol–gel synthesis. J Non Cryst Solids. 2007, 353(44–46):4102–7. https://doi.org/10.1016/J.JNONCRYSOL.2007.06.013
19. Murty BS, Yeh JW, Ranganathan S. High-entropy alloys. Oxford, UK: Butterworth-Heinemann Elsevier; 2014
20. Rost CM, Sachet E, Borman T, Moballegh A, Dickey EC, Hou D, et al. Entropy-stabilized oxides. Nat Commun. 2015, 6(1):1–8. https://doi.org/10.1038/ncomms9485
21. Musicó BL, Gilbert D, Ward TZ, Page K, George E, Yan J, et al. The emergent field of high entropy oxides: design, prospects, challenges, and opportunities for tailoring material properties. APL Mater. 2020, 8(4):040912. https://doi.org/10.1063/5.0003149
22. Zhao Z, Xiang H, Chen H, Dai F-Z, Wang X, Peng Z, et al. High-entropy (Nd0.2Sm0.2Eu0.2Y0.2Yb0.2)4Al2O9 with good high temperature stability, low thermal conductivity, and anisotropic thermal expansivity. J Adv Ceram. 2020, 9(5):595–605. https://doi.org/10.1007/S40145-020-0399-0
23. Tseng KP, Yang Q, McCormack SJ, Kriven WM. High-entropy, phase-constrained, lanthanide sesquioxide. J Am Ceram Soc. 2020, 103(1):569–76. https://doi.org/10.1111/jace.16689
24. Pianassola M, Anderson KL, Safin J, Agca C, McMurray JW, Chakoumakos BC, et al. Tuning the melting point and phase stability of rare-earth oxides facilitates their crystal growth from the melt. J Adv Ceram. 2022, 11(9):1479–90. https://doi.org/10.1007/s40145-022-0625-z
25. Pianassola M, Loveday M, Chakoumakos BC, Koschan M, Melcher CL, Zhuravleva M. Crystal growth and elemental homogeneity of the multicomponent rare-earth garnet (Lu1/6Y1/6Ho1/6Dy1/6Tb1/6Gd1/6)3Al5O12. Cryst Growth Des. 2020, 20(10):6769–76. https://doi.org/10.1021/acs.cgd.0c00887
26. Liu F, Dong L, Cao S, Chen J, Xu H, Han W, et al. Crystal growth, structural characterization and laser operation of an Yb0.19Y0.34Lu0.12Gd0.35Ca4O(BO3)3 mixed crystal. J Cryst Growth. 2021, 558:126023. https://doi.org/10.1016/j.jcrysgro.2020.126023

27. Pressley LA, Torrejon A, Phelan WA, McQueen TM. Discovery and single crystal growth of high entropy pyrochlores. Inorg Chem. 2020, 59(23):17251–8. https://doi.org/10.1021/acs.inorgchem.0c02479
28. Hines AT, Morrison G, Tisdale HB, Smith MD, Besmann TM, Mofrad A, et al. Crystallization of A3Ln(BO3)2(A = Na, K; Ln = lanthanide) from a boric acid containing hydroxide melt: synthesis and investigation of lanthanide borates as potential nuclear waste forms. Inorg Chem. 2022, 61(29):11232–42. https://doi.org/10.1021/ACS.INORGCHEM.2C01301/ASSET/IMAGES/LARGE/IC2C01301_0010.JPEG
29. Pianassola M, Stand L, Loveday M, Chakoumakos BC, Koschan M, Melcher CL, et al. Czochralski growth and characterization of the multicomponent garnet (Lu1/4Yb1/4Y1/4Gd1/4)3Al5O12. Phys Rev Mater. 2021, 5(8):083401. https://doi.org/10.1103/PhysRevMaterials.5.083401
30. Pianassola M, Alexander M, Chakoumakos B, Koschan M, Melcher C, Zhuravleva M. Effects of composition and growth parameters on phase formation in multicomponent aluminum garnet crystals. Acta Crystallogr B Struct Sci Cryst Eng Mater. 2022, 78:476–84. https://doi.org/10.1107/S2052520622002967/TQ5001SUP2.PDF
31. Pianassola M, Chakoumakos BC, Melcher CL, Zhuravleva M. Crystal growth and phase formation of high-entropy rare-earth aluminum perovskites. Cryst Growth Des. 2023, 23(1):480–88. https://doi.org/10.1021/acs.cgd.2c01130
32. Kinsler-Fedon C, Zheng Q, Huang Q, Choi ES, Yan J, Zhou H, et al. Synthesis, characterization, and single-crystal growth of a high-entropy rare-earth pyrochlore oxide. Phys Rev Mater. 2020, 4(10):104411. https://doi.org/10.1103/PhysRevMaterials.4.104411
33. Kinsler-Fedon C, Nuckols L, Nelson CT, Qi Z, Huang Q, Mandrus D, et al. Effects of Au2+ irradiation induced damage in a high-entropy pyrochlore oxide single crystal. Scr Mater. 2022, 220:114916. https://doi.org/10.1016/J.SCRIPTAMAT.2022.114916
34. Greculeasa M, Broasca A, Voicu F, Hau S, Croitoru G, Stanciu G, et al. Bifunctional LaxNdyGdzSc4−x−y−z(BO3)4 crystal: Czochralski growth, linear and nonlinear optical properties, and near-infrared laser emission performances. Opt Laser Technol. 2020, 131:106433. https://doi.org/10.1016/j.optlastec.2020.106433
35. Fukuda T, Chani VI. Shaped crystals: growth by the micro-pulling-down technique. Berlin, Heidelberg: Springer Berlin Heidelberg; 2007. https://doi.org/10.1007/978-3-540-71295-4
36. Toby BH, Von Dreele RB. GSAS-II: the genesis of a modern open-source all purpose crystallography software package. J Appl Crystallogr. 2013, 46(2):544–9. https://doi.org/10.1107/S0021889813003531
37. Zhu H, Liu L, Xiang H, Dai F-Z, Wang X, Ma Z, et al. Improved thermal stability and infrared emissivity of high-entropy REMgAl11O19 and LaMAl11O19 (RE = La, Nd, Gd, Sm, Pr, Dy; M = Mg, Fe, Co, Ni, Zn). J Mater Sci Technol. 2022, 104:131–44. https://doi.org/10.1016/J.JMST.2021.06.068
38. Song J, Cheng Y, Xiang H, Dai F-Z, Dong S, Chen G, et al. Medium and high-entropy transition mental disilicides with improved infrared emissivity for thermal protection applications. J Mater Sci Technol. 2023, 136:149–58. https://doi.org/10.1016/J.JMST.2022.07.028
39. De Graef M, McHenry ME. Structure of materials: an introduction to crystallography, diffraction and symmetry. Cambridge, UK: Cambridge University Press; 2012
40. Nagler SE, Stoica AD, Stoica GM, An K, Skorpenske HD, Rios O, et al. Time-of-flight neutron diffraction (TOF-ND) analyses of the composition and minting of ancient judaean "biblical" coins. J Anal Methods Chem. 2019, 2019:6164058. https://doi.org/10.1155/2019/6164058
41. Pianassola M, Anderson K, Agca C, Benmore CJ, McMurray JW, Neuefeind JC, et al. In situ high-temperature structural analysis of high-entropy rare-earth sesquioxides. Chem Mater. 2023, 35(3):1116–24. https://doi.org/10.1021/acs.chemmater.2c03088
42. Ushakov SV, Hayun S, Gong W, Navrotsky A. Thermal analysis of high entropy rare earth oxides. Mater. 2020, 13(14):3141. https://doi.org/10.3390/MA13143141
43. Agca C, Neuefeind JC, McMurray JW, Liu J, Benmore CJ, Weber RJK, et al. In situ high-temperature synchrotron diffraction studies of (Fe,Cr,Al)3O4 spinels. Inorg Chem. 2020, 59(9):5949–57. https://doi.org/10.1021/ACS.INORGCHEM.9B03726
44. Skinner LB, Benmore CJ, Weber JKR, Tumber S, Lazareva L, Neuefeind J, et al. Structure of molten CaSiO3: neutron diffraction isotope substitution with aerodynamic levitation and molecular dynamics study. J Phys Chem B. 2012, 116(45):13439–47. https://doi.org/10.1021/JP3066019
45. Neuefeind J, Feygenson M, Carruth J, Hoffmann R, Chipley KK. The nanoscale ordered materials diffractometer NOMAD at the spallation neutron source SNS. Nucl Instruments Methods Phys Res Sect B Beam Interact with Mater Atoms. 2012, 287:68–75. https://doi.org/10.1016/J.NIMB.2012.05.037
46. Agca C, Neuefeind JC, McMurray JW, Weber R, Navrotsky A. Melting temperature measurement of refractory oxide ceramics as a function of oxygen fugacity using containerless methods. J Am Ceram Soc. 2020, 103(9):4867–75. https://doi.org/10.1111/JACE.17216
47. Weber R, Wilke SK, Benmore CJ. Containerless techniques for in-situ X-ray measurements on materials in extreme conditions. J Phys Soc Japan. 2022, 91:091008. https://doi.org/10.7566/JPSJ.91.091008
48. Sontakke AD, Ueda J, Katayama Y, Zhuang Y, Dorenbos P, Tanabe S. Role of electron transfer in Ce3+ sensitized Yb3+ luminescence in borate glass. J Appl Phys. 2015, 117(1):013105. https://doi.org/10.1063/1.4905317
49. Li H, Li W, Gu S, Wang F, Zhou H, Liu X, et al. Enhancement of photocatalytic activity in Tb/Eu co-doped Bi 2 MoO 6 : the synergistic effect of Tb–Eu redox cycles. RSC Adv. 2016, 6(53):48089–98. https://doi.org/10.1039/C6RA08739F

SUPPORTING INFORMATION

Additional supporting information can be found online in the Supporting Information section at the end of this article.

How to cite this article: Pianassola M, Loveday M, Lalk R, Pestovich K, Melcher CL, Zhuravleva M. Crystal growth and phase formation of high-entropy rare-earth monoclinic aluminates. J Am Ceram Soc. 2023;1–10. https://doi.org/10.1111/jace.19320